FRONTIERS OF PHYSICS

RESEARCH ARTICLE
Volume 18 / Issue 3 / 33307 / 2023

Reversible doping polarity and ultrahigh carrier density in two-dimensional van der Waals ferroelectric heterostructures

Yanyan Li[1], Mingjun Yang[1], Yanan Lu[1], Dan Cao[2], Xiaoshuang Chen[3], Haibo Shu[1,†]

1 College of Optical and Electronic Technology, China Jiliang University, Hangzhou 310018, China
2 College of Science, China Jiliang University, Hangzhou 310018, China
3 National Laboratory for Infrared Physics, Shanghai Institute of Technical Physics, Chinese Academy of Science, Shanghai 200083, China
Corresponding author. E-mail: †shuhaibo@cjlu.edu.cn
Received May 22, 2022; accepted September 5, 2022

ABSTRACT

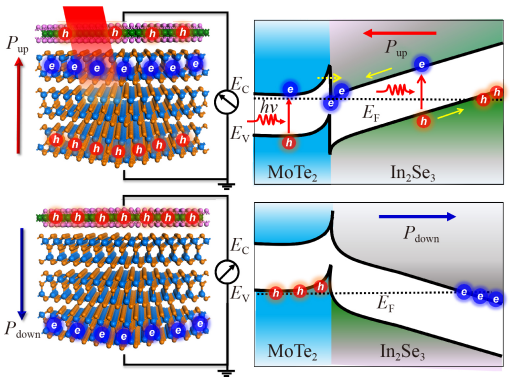

Van der Waals semiconductor heterostructures (VSHs) composed of two or more two-dimensional (2D) materials with different band gaps exhibit huge potential for exploiting high-performance multifunctional devices. The application of 2D VSHs in atomically thin devices highly depends on the control of their carrier type and density. Herein, on the basis of comprehensive first-principles calculations, we report a new strategy to manipulate the doping polarity and carrier density in a class of 2D VSHs consisting of atomically thin transition metal dichalcogenides (TMDs) and α-In_2X_3 (X = S, Se) ferroelectrics via switchable polarization field. Our calculated results indicate that the band bending of In_2X_3 layer driven by the FE polarization can be utilized for engineering the band alignment and doping polarity of TMD/In_2X_3 VSHs, which enables us to control their carrier density and type of the VSHs by the orientation and magnitude of local FE polarization field. Inspired by these findings, we demonstrate that doping-free p–n junctions achieved in $MoTe_2/In_2Se_3$ VSHs exhibit high carrier density (10^{13}–10^{14} cm^{-2}), and the inversion of the VHSs from n–p junctions to p–i–n junctions has been realized by the polarization switching from upward to downward states. This work provides a nonvolatile and nondestructive doping strategy for obtaining programmable p–n van der Waals (vdW) junctions and opens the possibilities for self-powered and multifunctional device applications.

Keywords van der Waals heterostructures, ferroelectric polarization, carrier type, band alignment, density-functional theory

1 Introduction

Semiconductor heterostructures (SHSs) are a basic building block for electronic and optoelectronic devices since they not only combine the properties and functionalities of constituent materials but also exhibit various exotic effects due to the interfacial interactions [1–3]. Traditional synthetic methods of SHSs, such as chemical and physical epitaxial growth, suffer from the limitation of lattice mismatch that easily leads to the formation of interface defects and lattice disorders, which greatly restricts their device applications [4, 5]. Emerging 2D layered semiconductor materials, such as transition metal dichalcogenides (TMD) [6, 7], black phosphorus

Higher Education Press

https://doi.org/10.1007/s11467-022-1244-4

(BP) [8], and group-VA elements and compounds [9], provide a state-of-the-art approach to design SHSs via van der Waals (vdW) integration. Owing to the dangling-bond-free surface with weak interlayer interactions, the integration of these 2D materials into vdW semiconductor heterostructures (VSHs) without the limitation of lattice mismatch. Hence, VSHs offer a large degree of freedom for the device design with desired interface structures and band alignments and become an ideal platform for exploring novel physical properties [10, 11]. A typical example is twisted TMD VSHs that possess unconventional moiré excitons and charge density wave (CDW) state [12, 13]. Great achievements have been made in the last years on the synthesis of 2D VSHs, such as MoS_2/WS_2 [14], $MoSe_2/WSe_2$ [15], SnSe/MoS_2 [16], and SnS/SnS_2 [17], and BP/MoS_2 [18]. 2D VSHs exhibit huge potential for nanoelectronics and optoelectronics, including light emitting diodes, field-effect transistors, photodetectors, memories, lasers, and solar cells, etc. [19, 20].

The device applications of 2D VSHs depend on the manipulation of the type, density, and spatial distribution of charge carriers. The impurity doping is the most common way to produce charge carriers by means of intentional introduction of impurity atoms into the host lattice. However, this approach implemented in 2D semiconductors remains a large challenge due to their ultrathin atomic structures and limited physical space [21]. In particular for the heavy doping, excessive incorporation of impurities into 2D host lattices easily causes severe structural damage and lattice disorder [22]. Therefore, various new doping strategies were developed to program the carrier type and concentration of 2D materials, including chemical intercalation [23], surface charge transfer [24], electron-beam irradiation [25], laser light illumination [26], and electrostatic doping [27, 28]. However, most of these doping methods inevitably introduce chemical species or induce the formation of lattice defects [23–26], consequently resulting in the degeneration of device performance. Moreover, the polarity and transfer characteristics of p–n junctions are difficult to be changed once these doping methods have been implemented in 2D semiconductors and VSHs [29]. Although the gate-tuned electrostatic doping method provides a flexible way to tune the charge carriers, it requires an additional voltage to maintain the type and density of carriers therefore is volatile [30]. Hence, the development of nonvolatile and nondestructive doping ways to realize p-n junctions in atomically thin semiconductor materials is highly desired.

Because of atomic-scale thickness and ultraflat surface, the band structures of 2D vdW crystals and heterostructures are sensitive to the modulation of external and local electric fields. Considering that an external electric field cannot provide a nonvolatile doping way for the control of charge carriers, the creation of a local electric field is an alternative strategy to achieve this goal. Ferroelectric materials possess a spontaneous polarization that can be reversed by an electric field stimulus. Therefore, the integration of 2D semiconductors on ferroelectric (FE) substrates create a local and nonvolatile electric polarization field at the interface [31], which can be used to modulate the carrier type and density of 2D channel materials without sacrifice of their intrinsic physical properties. For example, the selective p- and n-type doping in atomically thin TMDs such as MoS_2, $MoTe_2$, and WSe_2 have been demonstrated on a series of FE substrates, including $BiFeO_3$ [32], $PbTiZrO_3$ [33], $LiNbO_3$ [34], $Na_{0.5}Bi_{4.5}Ti_4O_{15}$ [35], and P(VDF-FrFE) [36, 37]. However, most of FE materials require a large thin-film thickness to maintain their polarization due to the depolarization field effect [38], which is incompatible with the trend of device minimization. Moreover, the insulator nature of FE oxides with large band gap (> 3.5 eV) [39] makes them difficult to be integrated into SHSs as the channel materials for device applications. Instead, the rapid development of 2D layered FE materials such as $CuInP_2S_6$ [40], In_2Se_3 [41], SnS [42], and $MoTe_2$ [43] brings new possibility for the realization of nonvolatile doping by means of a local electric polarization field. Some 2D ferroelectrics exhibit robust spontaneous polarization down to single-layer limit [42–44]. Especially for 2D α-In_2X_3 (X = S, Se) ferroelectrics, they are semiconductors with the band gap range of 1.4–2.8 eV [45]. Therefore, the combination of 2D semiconductors (e.g., TMDs and BP) with α-In_2X_3 ferroelectrics into FE VSHs can induce several aspects of advantages compared with other types of SHSs. (i) The dangling-bond-free surfaces lead to the formation of VSHs with a sharp atomic interface that is conductive to the doping modulation by the local polarization-field. (ii) The switchable FE field can be used to engineer the band alignment of the VSHs, including type-I (straddling gap), type-II (staggered gap), and type-III (broken gap) [46], which is essential for exploiting multifunctional devices. (iii) The ultrathin structure of FE VSHs is adapted to the trend of device minimization. Although the FE polarization field has been confirmed as a feasible way for regulating the carrier density and type in 2D semiconductors, the FE polarization effect on the band alignment, doping polarity, and carrier density in 2D FE VSHs remains unexplored.

In this work, we report a nonvolatile doping strategy in 2D ferroelectric VSHs consisted of TMD monolayers ($MoSe_2$ and $MoTe_2$) and experimentally available α-In_2X_3 (X = S, Se) nanosheets. The local FE polarization-field effect on the band alignment and carrier density of TMD/In_2X_3 VSHs is systematically studied by the first-principles calculations. Different from conventional 2D semiconductors, there is a layer-by-layer band shift in α-In_2X_3 semiconductors induced by the FE polarization field, which creates a favorable condition for the modulation of band alignment and carrier density in TMD/In_2X_3

VSHs. We demonstrate that free-doping and nonvolatile p–n or p–i–n junctions with ultrahigh carrier concentration (10^{13}–10^{14} cm^{-2}) can be achieved in $MoTe_2/In_2Se_3$ VSHs, and their carrier type and spatial distribution can be modulated by the control of FE polarization states. These findings suggest huge potential of 2D $MoTe_2/In_2Se_3$ VSHs for self-powered multifunctional device applications.

2 Methods

2.1 Computational details

All density functional theory (DFT) calculations were performed in the Vienna ab initio Simulation Package (VASP) code with the projector augmented wave (PAW) method [47]. The electronic exchange-correlation energy was treated by the generalized-gradient approximation (GGA) functional in the form of Perdew–Burke–Ernzerh (PBE) [48]. The vdW interactions were treated with the DFT-D3 correction in Grimme's scheme [49]. A kinetic energy cutoff was set to 500 eV for the plane-wave expansion set. A vacuum layer of more than 20 Å along the z-axis (or out-of-plane) direction was added to avoid the interactions between adjacent periodic slabs. Since the PBE functional usually underestimates the band gap of semiconductors, electronic structures of all 2D structures were predicted by the hybrid functional of Heyd–Scuseria–Ernzerhof (HSE06) [50]. The dipole correction along the z-axis direction was adopted to meet the convergence criterion. The Monkhorst–Pack scheme was used for the k-point sampling in the Brillouin zone with the grid of 16 × 16 × 1 for 2D materials and 12 × 12 × 1 for 2D VSHs, respectively. All geometry optimization was carried out using the conjugate-gradient method and the convergence criteria of energy and force was set to 10^{-4} eV/atom and 10^{-2} eV/Å, respectively. The out-of-plane electric polarization was evaluated by using the Berry phase method [51]. Bader charge analysis was performed to examine the interfacial charge transfers [52].

2.2 Heterostructure models

Prior to constructing In_2X_3/TMD (X = S, Se) VSHs, the geometrics of 2D freestanding TMD monolayers (i.e., $MoSe_2$ and $MoTe_2$) and α-In_2X_3 (X = S, Se) were firstly optimized. For hexagonal H-phase TMD monolayers, the optimized in-plane lattice constant a is 3.32 Å and 3.55 Å for the monolayer $MoSe_2$ and $MoTe_2$, respectively. α-In_2X_3 (X = S, Se) nanosheets also possess hexagonal lattice with the atom sequence of Se–In–Se–In–Se in each layer. The optimized lattice constant a is 3.95 Å and 4.11 Å for α-In_2S_3 and α-In_2Se_3, respectively. The increase of layer number from the monolayer to tetralayer brings few changes of the in-plane lattice constants (< 0.1 Å). Based on the optimized 2D freestanding structures, 2D In_2X_3/TMD VSHs were created by vertically stacking a (2 × 2) TMD monolayer on a ($\sqrt{3}$ × $\sqrt{3}$) α-In_2X_3 nanosheet, which makes that the lattice mismatch of all considered VSHs is less than 2.7%. According to the polarization orientation, TMD/In_2X_3 VSHs were classed into TMD/In_2X_3(↑) and TMD/In_2X_3(↓), respectively. The optimal interfacial configuration of each In_2X_3/TMD VSH was obtained by the energy comparison [see Fig. S1 in the Electronic Supplementary Material (ESM) for details]. The interfacial interactions of the VSHs were determined by calculating interfacial binding energies (γ_{int}) as follows:

$$\gamma_{int} = (E_{tot} - E_{TMD} - E_{In_2X_3})/S_A, \quad (1)$$

where E_{tot}, E_{TMD}, $E_{In_2X_3}$ are the total energies of a given In_2X_3/TMD VSH, monolayer TMD monolayer, and α-In_2X_3 nanosheet, respectively, S_A is the interfacial area. The optimized lattice parameters and energetic data of $MoTe_2/In_2Se_3$ and $MoSe_2/In_2S_3$ VSHs were listed in Tables S1 and S2 of the ESM, respectively.

2.3 Calculation of carrier density

The carrier density of electrons (σ_n) and holes (σ_p) in 2D semiconductors and VSHs was determined as follows [46]:

$$\sigma_n = \frac{4\pi m_e^* kT}{h^2} \ln\left[1 + \exp\left(\frac{E_F - E_C}{kT}\right)\right], \quad (2)$$

$$\sigma_p = \frac{4\pi m_h^* kT}{h^2} \ln\left[1 + \exp\left(\frac{E_V - E_F}{kT}\right)\right], \quad (3)$$

where m_e^* (m_h^*) is electron (hole) effective mass, T is the temperature, k is Boltzmann constant, h is Plank constant. E_F–E_C and E_V–E_F are the separation from Fermi level to CBM and VBM, respectively, and they can be directly extracted from the calculated band structures. The m_e^* and m_h^* were calculated from the band curvature at the CBM and VBM, respectively, by using the following formula [46]:

$$\frac{1}{m^*} = \frac{1}{\hbar^2}\frac{d^2E(k)}{dk^2}, \quad (4)$$

where $E(k)$ is the energy of band-edge states (VBM and CBM) at wave-vector k, and $\hbar$ is the reduced Plank constant.

3 Results and discussion

3.1 Polarization effect on electronic properties of 2D In_2X_3 ferroelectrics

Before addressing the FE polarization effect on the band

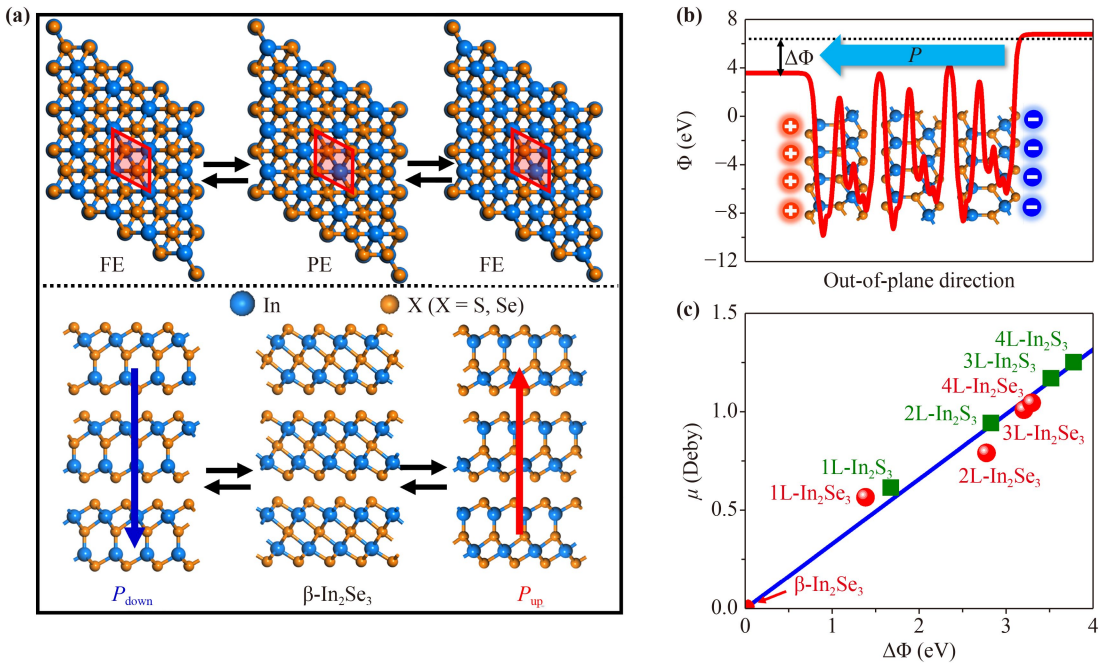

Fig. 1 Atomic structures and intrinsic polarization of 2D α-In_2X_3 ferroelectrics. **(a)** Top and side views of the atomic structure of trilayer In_2X_3 nanosheets in FE and PE phases. The arrows ↓ and ↑ denote the ferroelectric α-In_2X_3 nanosheet in P_{down} and P_{up} states, respectively. The rhombic frames represent the range of a unit cell. The blue and orange balls denote In and X atoms, respectively. **(b)** The average EPD (Φ) of a trilayer α-In_2Se_3 along the out-of-plane direction. Here ΔΦ denotes the electrostatic potential difference between two surface terminations. **(c)** The μ of 2D α-In_2X_3 ferroelectrics as a function of ΔΦ.

alignment and carrier density of 2D TMD/In_2X_3 VSHs, it is necessary to first understand ferroelectric and electronic properties of 2D layered α-In_2X_3 (X = S, Se) nanosheets. Figure 1(a) shows atomic structures of In_2X_3 nanosheets in α and β phases. The α-In_2X_3 nanosheets have a hexagonal lattice with asymmetric distribution of X–In–X–In–X atomic layers in each In_2X_3 sheet that causes spontaneously aligned electric dipoles along the out-of-plane direction, which is responsible for the formation of FE polarization. According to the polar-axis orientation, the FE polarization can be divided into downward and upward states (P_{down} and P_{up}), respectively. In contrast, the X–In–X–In–X atomic arrangement in β-In_2X_3 nanosheets is spatially symmetric along the out-of-plane direction [Fig. 1(a)], which makes β-In_2X_3 nanosheets as paraelectric (PE) phase without spontaneous polarization. When α-In_2X_3 nanosheets are loaded by an external electric field, their polarization orientation can be switched between the P_{down} and P_{up} states via the PE phase. The intrinsic FE polarization leads to a build-in electrostatic field in α-In_2X_3 along the out-of-plane direction, which can be confirmed by electrostatic potential distributions (EPDs). The electrostatic potential (Φ) of a trilayer (3L) α-In_2Se_3 nanosheet shows an asymmetric distribution [Fig. 1(b)], resulting in an electrostatic potential difference (ΔΦ) of 3.20 eV between two surface terminations and electric dipole moment (μ) of 1.01 Deby. The similar results have been appeared in other 2D α-In_2X_3 (Fig. S2 in the ESM). For β-In_2Se_3 nanosheets, their Φ shows completely a symmetric distribution along the out-of-plane direction (Fig. S3 in the ESM) and corresponding ΔΦ and μ values are zero. Hence, ΔΦ and μ values reflect the magnitude of spontaneous polarization in In_2X_3 ferroelectrics. We plot the μ of eight 2D α-In_2X_3 as a function of ΔΦ in Fig. 1(c). There is a nearly linear relationship between ΔΦ and μ, and it can be fitted by an expression $\mu = 0.33\Delta\Phi$. So a large ΔΦ means the accumulation of more surface dipole charges, which corresponds to a large polarization field. Hence, the intrinsic polarization of α-In_2S_3 is correspondingly stronger than that of α-In_2Se_3. For example, based on Berry-phase method [51], the intrinsic polarization (P) is 1.41 μC/cm^2 and 1.09 μC/cm^2 for monolayer α-In_2S_3 and α-In_2Se_3, respectively. In addition, the increase of layer number leads to the increase of ΔΦ and μ values in 2D α-In_2X_3 ferroelectrics. Nevertheless, the ΔΦ and μ values are gradually saturated when the layer number is beyond 3L (Fig. S4 in the ESM), which agrees well with previous report about the thickness-dependent polarization in 2D α-In_2Se_3 [53].

The local FE polarization-field effect on electronic properties of 2D α-In_2X_3 is evaluated by their band structures and density of states (DOS) obtained by the HSE06 functional. Figure 2(a) presents the projected

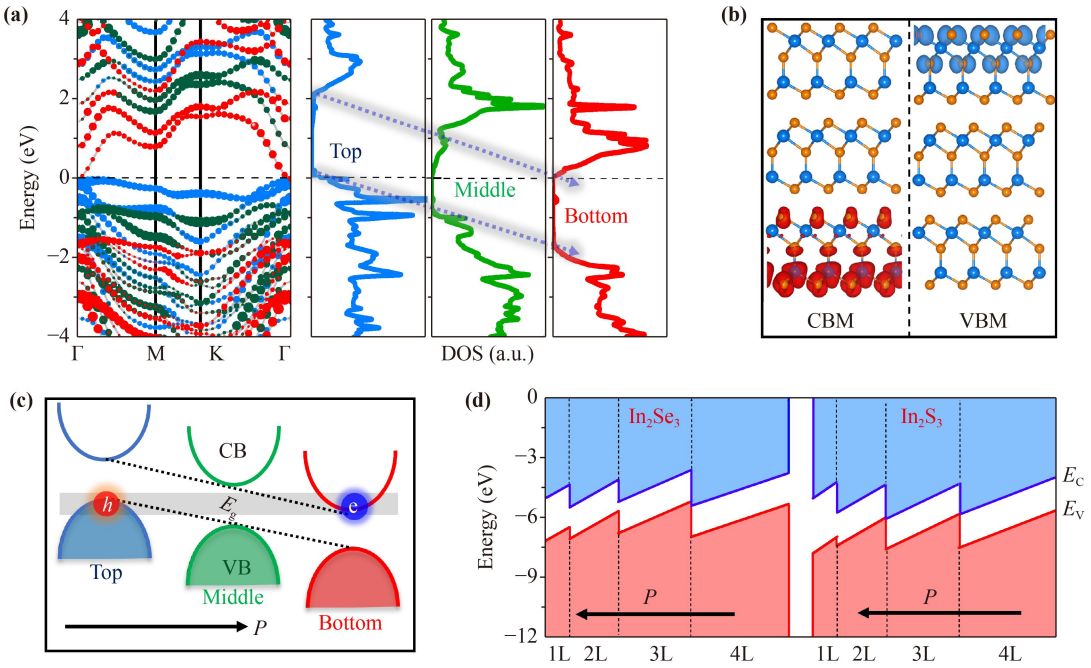

Fig. 2 Polarization effect on electronic properties of 2D α-In_2X_3 nanosheets. **(a)** Projected band structure and DOS of a trilayer α-In_2Se_3 nanosheet obtained by the HSE06 functional. The Fermi level is set to the energy zero point. **(b)** Charge density isosurfaces of CBM and VBM states in the trilayer α-In_2Se_3 nanosheet. **(c)** Schematic of the polarization-induced layer-by-layer band shift in a trilayer α-In_2X_3 nanosheet. **(d)** Band-edge energies of eight 2D α-In_2X_3 structures relative to the vacuum level. E_C and E_V correspond to the energy of CBM and VBM, respectively. The arrows indicate the polarization direction.

band structure and DOS of a trilayer α-In_2Se_3. It seems that it is a metal due to the lack of band gap. Actually, each In_2Se_3 layer in the trilayer structure remains semiconducting characteristic with the band gap values of 1.4–1.5 eV, but there is a layer-by-layer band shift [Fig. 2(a)]. More specifically, the top-layer bands indicate a notable upward shift relative to the bottom-layer ones when the polarization direction points from the bottom layer to the top layer. The charge-density isosurface distributions of the trilayer α-In_2Se_3 display that its conduction band minimum (CBM) and valence band maximum (VBM) are dominated by the bottom-layer and top-layer electronic states [Fig. 2(b)], respectively. The result confirms the layer-by-layer band shift induced by the polarization field [i.e., so-called quantum-confined Stark (QCS) effect] that drives the separation of electron and hole wave functions. Hence, there is an inclined band structure or band bending in the trilayer α-In_2Se_3 nanosheet [Fig. 2(c)]. Similar results can be also found in other 2D α-In_2X_3 structures (Fig. S5 in the ESM).

In order to offer a comprehensive understanding of the polarization effect on the band alignment of 2D α-In_2X_3 ferroelectrics, their band-edge energies (E_C and E_V) relative to the vacuum level are plotted in Fig. 2(d). Different from the conventional 2D semiconductors (e.g., TMDs), all 2D α-In_2X_3 (X = S, Se) structures possess inclined band alignment along the direction of polar axis. Their band gaps (E_g) show a rapid reduction with increasing layer number due to the cooperation of quantum size effect and QCS effect. For example, the E_g is 1.43, 0.11, and 0 eV for the monolayer (1L), bilayer (2L), and trilayer (3L) α-In_2Se_3, respectively. Moreover, the VBM energy of top-layer In_2X_3 is higher than the CBM energy of bottom-layer In_2X_3 when the thickness is beyond 2L due to the layer-by-layer band shift, consequently leading to the formation of self-doped p–n junctions in 2D α-In_2X_3 [54]. Moreover, the self-doping characteristics can be stabilized even if the layer thickness is further increased due to the Fermi-level pinning caused by the crossover of band-edge states between the top and bottom layers.

3.2 Band alignments and tunable carrier types in TMD/In_2X_3 VSHs

Thanks to the polarization-induced band bending (or layer-by-layer band shift) in 2D α-In_2X_3 (X = S, Se) ferroelectrics, the integration of them with the conventional 2D semiconductors (e.g., $MoSe_2$ and $MoTe_2$) creates the possibility to control their band alignments and carrier distribution via switchable FE polarization. We selected 2D $MoTe_2/In_2Se_3$ VSHs as an example to demonstrate the polarization-field effect on their electronic structures

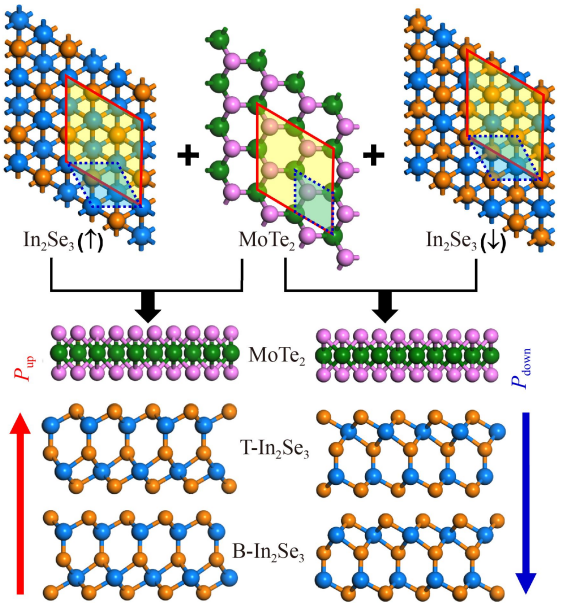

Fig. 3 Top and side views of the atomic structure of 2D $MoTe_2/In_2Se_3$ VSHs in P_{down} and P_{up} states. The solid frames denote the supercells of α-In_2Se_3 and $MoTe_2$ used for the construction of VSHs, and the dash frames denote the primitive cell of α-In_2Se_3 and $MoTe_2$. T-In_2Se_3 and B-In_2Se_3 denote the top-layer and bottom-layer In_2Se_3, respectively.

and doping polarity, and the thickness of α-In_2Se_3 layer in the VHSs is considered from 1L to 4L. The VSHs were constructed by vertically stacking a 2 × 2 $MoTe_2$ monolayer on $\sqrt{3} \times \sqrt{3}$ α-In_2Se_3 nanosheets for the minimization of lattice mismatch. Based on the polar-axis orientation (P_{down} and P_{up}), the VSHs were classified into $MoTe_2/In_2Se_3(\downarrow)$ and $MoTe_2/In_2Se_3(\uparrow)$ (Fig. 3). The interfacial structure of each VSH was determined by the energy comparison among six potential interfacial configurations (see Fig. S1 in the ESM for details), and the most stable one was selected for the study of electronic properties. The optimized lattice and energetic parameters of the lowest-energy VSHs in P_{down} and P_{up} states are listed in Tables S1 and S2. All $MoTe_2/In_2Se_3$ VSHs have negative interfacial binding energies (γ_{int}), indicating that the formation of vdW heterojunctions is energetically favorable. Moreover, the γ_{int} values of these VSHs (–0.32– –0.45 J/m^2) are comparable with other 2D vdW crystals (–0.2– –0.5 J/m^2) [55], indicating the heterointerfaces are interacted by the vdW force. By comparison, the γ_{int} of $MoTe_2/In_2Se_3(\downarrow)$ VSHs is correspondingly larger than that of $MoTe_2/In_2Se_3(\uparrow)$ ones, resulting in relatively small interlayer distances (d = 3.39–3.44 Å) in $MoTe_2/In_2Se_3(\downarrow)$ VSHs due to stronger interfacial interactions. The difference of interfacial interactions between the two types of VSHs plays an important role in the determinization of their band alignments, which will be discussed later.

We now turn to reveal the local polarization-field effect on the band alignment of 2D $MoTe_2/In_2Se_3$ VSHs. Figure 4 shows the projected band structures and DOS of $MoTe_2/In_2Se_3(\uparrow)$ VSHs calculated by the HSE06 functional. For $MoTe_2$/1L-$In_2Se_3(\uparrow)$ VSH [Fig. 4(a)], it

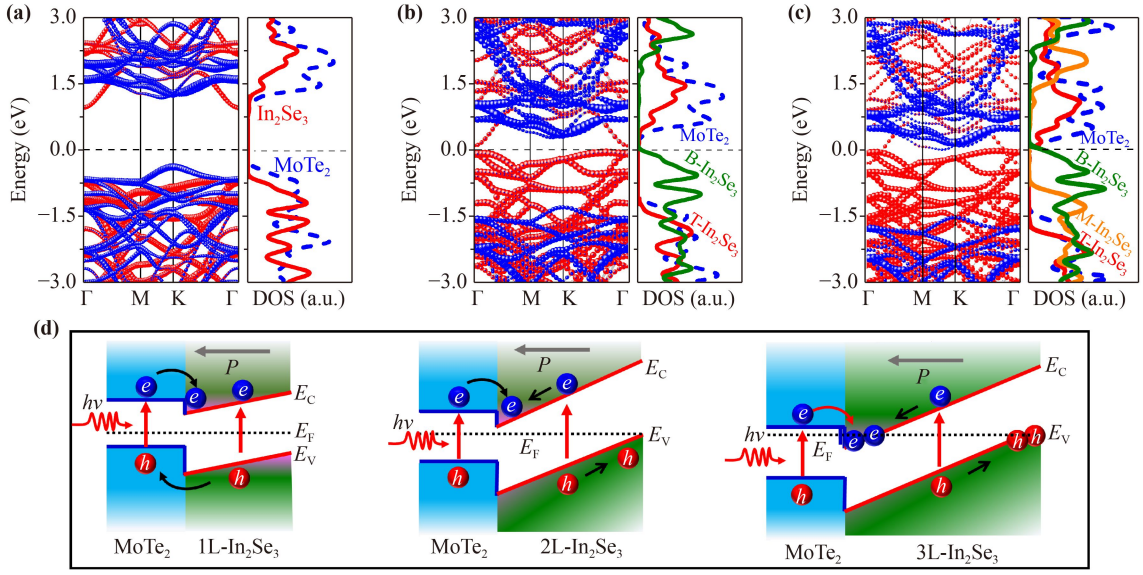

Fig. 4 Band alignments of 2D $MoTe_2/In_2Se_3(\uparrow)$ VSHs with the thickness range of In_2Se_3 layer from 1L to 3L. **(a–c)** Projected band structure and DOS of VSH with (a) 1L-In_2Se_3, (b) 2L-In_2Se_3, and (c) 3L-In_2Se_3. The red and blue bands denote the contribution from In_2Se_3 and $MoTe_2$ layers, respectively. The horizontal dash lines denote the position of Fermi level. T-In_2Se_3, M-In_2Se_3, and B-In_2Se_3 represent the top-layer, middle-layer, and bottom-layer In_2Se_3 in the VSHs, respectively. **(d)** Schematic of band alignments of $MoTe_2/In_2Se_3(\uparrow)$ VSHs. The black and gray arrows denote the carrier transport direction and polarization direction, respectively.

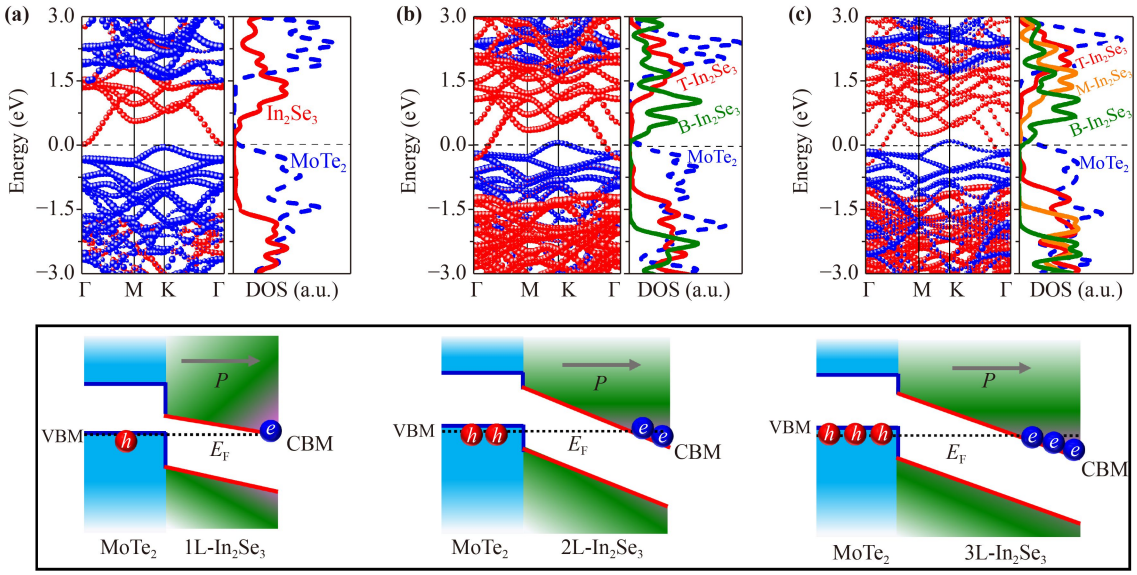

Fig. 5 Band alignments of 2D $MoTe_2/In_2Se_3(\downarrow)$ VSHs with the thickness range of In_2Se_3 layer from 1L to 3L. **(a–c)** Projected band structure and DOS of VSH with (a) 1L-In_2Se_3, (b) 2L-In_2Se_3, and (c) 3L-In_2Se_3. The red and blue bands represent the contribution of In_2Se_3 and $MoTe_2$ layers, respectively. The horizontal dash lines denote the position of Fermi level. T-In_2Se_3, M-In_2Se_3, and B-In_2Se_3 represent the top-layer, middle-layer, and bottom-layer In_2Se_3 in the VSHs, respectively. **(d)** Schematic of band alignments of $MoTe_2/In_2Se_3(\downarrow)$ VSHs. The arrows indicate the polarization direction.

exhibits a typical type-II band alignment in which the CBM and VBM states are contributed by the α-In_2Se_3 and $MoTe_2$ layers, respectively. The thickness increase in In_2Se_3 layer brings two notable changes in band structures [Figs. 4(a)–(c)]: (i) the band gap of In_2Se_3 layer rapidly decrease and disappear due to the size and QCS effects, (ii) the $MoTe_2$-layer bands show a downward shift towards the low-energy direction. It seems that the increase of In_2Se_3 layer induces the band-alignment transition from the type-II to type-I, to metallic, but the results of projected DOS indicate that the interfacial band alignment of all the VSHs possesses the type-II characteristic. For example, for $MoTe_2/2L\text{-}In_2Se_3(\uparrow)$ VSH, the band-edge states of the top-layer In_2Se_3 (T-In_2Se_3) and $MoTe_2$ layer exhibit a staggered distribution, indicating the type-II band alignment [Fig. 4(b)]. Similar result has also been appeared in other VSHs in P_{up} state. The band bending of In_2Se_3 layer induced by the polarization field makes the electron accumulation at T-In_2Se_3 near the interface of VSHs, especially for the light irradiation condition [Fig. 4(d)]. Owing to the existence of build-in electric field, the thickness increase of In_2Se_3 layer will drive the separation of electrons and holes onto T-In_2Se_3 and B-In_2Se_3, respectively. Moreover, the carrier density of the VSHs can be enhanced by the thickness increase of In_2Se_3 layer, resulting in the formation of self-doped p–n junctions in the In_2Se_3 layer. Nevertheless, the distribution of band-edge states in $MoTe_2/In_2Se_3(\uparrow)$ VSHs has few changes when the thickness of In_2Se_3 layer is beyond 3L (Fig. S6 in the ESM), which arises from the crossover of band-edge states. Therefore, the band alignment and doping polarity of the VSHs will be similar to that of $MoTe_2/3L\text{-}In_2Se_3(\uparrow)$ VSH [Fig. 4(c)] even if the thickness of In_2Se_3 layer is further increased.

Figure 5 displays the project band structures and DOS of $MoTe_2/In_2Se_3(\downarrow)$ VSHs. Contrary to the case of $MoTe_2/In_2Se_3(\uparrow)$ VSHs, the CB- and VB-edge states of $MoTe_2/In_2Se_3(\downarrow)$ VSHs are contributed by the B-In_2Se_3 and $MoTe_2$ layers, respectively. The CBM positions of all these VSHs are lower than the Fermi level and their VBM positions are higher than the Fermi level, leading to the formation of p-$MoTe_2/n$-In_2Se_3 vdW junctions. Interestingly, all these VSHs have type-II interface band alignment based on the result of projected DOS. Different from the conventional type-II SHSs, the electrons and holes can be rapidly separated into two surface terminations of the VSHs due to the effect of FE polarization field. Hence, the VSHs behave as self-doped p–i–n junction along the polarization direction [Fig. 5 (d)]. The tunable band alignments and self-doping characteristic have been also found in 2D $MoSe_2/In_2S_3$ VSHs (see Figs. S7 and S8 in the ESM), suggesting that the FE polarization field can be regarded as an efficient way to tune the carrier type and density in 2D ferroelectric VSHs.

In order to reveal the effect of FE polarization on the band alignment and doping polarity of $MoTe_2/In_2Se_3$ VSHs, their EPDs and interface charge transfers have been investigated. Figure 6(a) indicates the EPDs of $MoTe_2/3L\text{-}In_2Se_3$ VSH in two polarization states. The electrostatic potentials (Φ) at two surface terminations of the VSHs are different due to the existence of a polar-

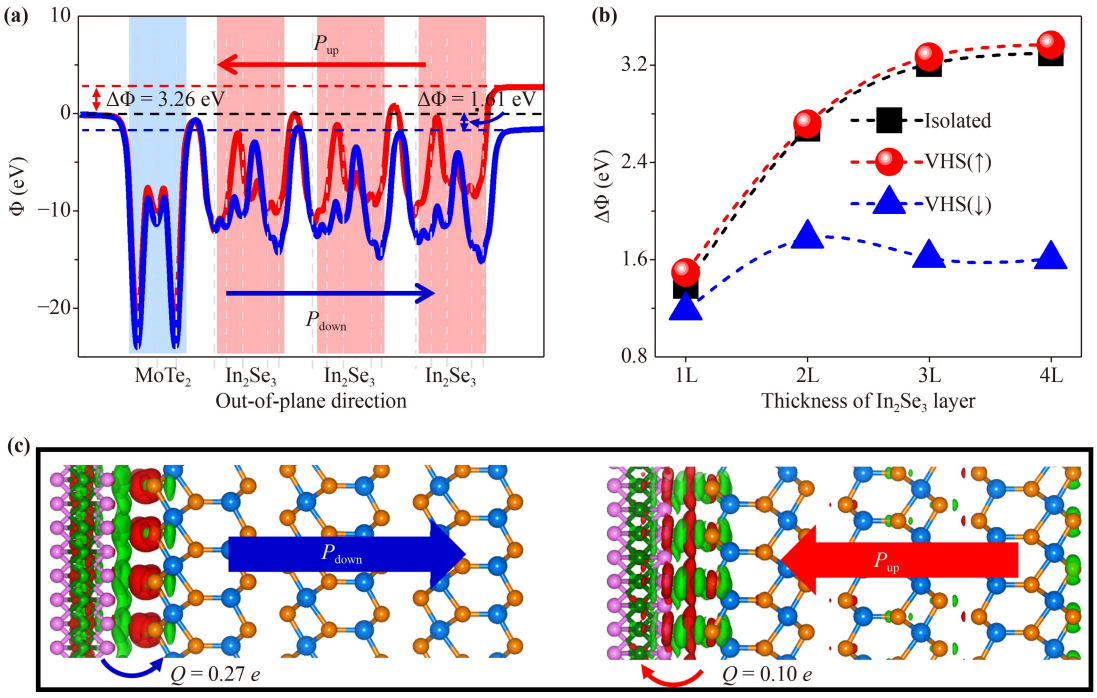

Fig. 6 Average electrostatic potential (Φ) and interfacial charge transfer of $MoTe_2/In_2Se_3$ VSHs. **(a)** Electrostatic potential distribution of $MoTe_2$/3L-In_2Se_3 VSH in P_{up} (red line) and P_{down} (blue line) states. **(b)** Electrostatic potential differences (ΔΦ) of $MoTe_2/In_2Se_3$ VSHs and isolated In_2Se_3 nanosheets as a function of In_2Se_3 layer thickness. **(c)** The charge-density difference and interfacial charge transfer (Q) of $MoTe_2$/3L-In_2Se_3 VSH in P_{down} (left) and P_{up} (right) state.

ization field. The calculated ΔΦ of $MoTe_2$/3L-In_2Se_3(↑) VSH (3.26 eV) largely approaches that of freestanding 3L-In_2Se_3 (3.20 eV) but is far large than that of $MoTe_2$/3L-In_2Se_3(↑) VSH (1.61 eV). Similar results can be also found in other VSHs [Fig. 6(b)]. The reduction of ΔΦ implies that the polarized charges of In_2Se_3 layer have been partially counteracted by interfacial charge transfers, weakening the FE polarization field [56]. To examine the interfacial charge transfers, the differential charge densities of $MoTe_2$/3L-In_2Se_3 VSHs in two polarization states have been calculated [Fig. 6(c)]. The red and green charge-density isosurfaces denote the charge accumulation and depletion, respectively. It can be clearly identified the charge localization at T-In_2Se_3 and the charge depletion at the $MoTe_2$ layer for the VSH in P_{down} state, corresponding to the electron transfer (~0.27 e) from the $MoTe_2$ layer to T-In_2Se_3 based on the analysis of Bader charges. In contrast, the charge accumulation and depletion at the interface of $MoTe_2$/3L-In_2Se_3 in P_{up} state are relatively small. Bader analysis shows few charge transfers (~0.1 e) from the T-In_2Se_3 layer to the $MoTe_2$ layer. In addition to the charge transfers, the interfacial electron tunneling is another important factor for the change of ΔΦ in the VSHs. For the VSHs in P_{up} state, they present the type-II band alignment [Fig. 4(d)]. Hence, the valence electrons of the $MoTe_2$ layer cannot spontaneously transfer into the In_2Se_3 layer due to the interfacial energy barriers. This is the reason why the layer-dependent ΔΦ of $MoTe_2/In_2Se_3$(↑) VSHs is very similar to that of the isolated α-In_2Se_3. In contrast, for the VSHs in P_{down} state, the CBM position of the bottom-layer In_2Se_3 is lower than the VBM position of the $MoTe_2$ layer when the layer number of In_2Se_3 is beyond 1L [Fig. 5(d)], resulting in a type-III band alignment between the bottom-layer In_2Se_3 and the $MoTe_2$ layer. Hence, the electrons can be tunneled from the $MoTe_2$ layer into the In_2Se_3 layer, which weakens the FE polarization field. Therefore, the ΔΦ values of $MoTe_2/In_2Se_3$(↓) VSHs are far smaller than those of the isolated α-In_2Se_3. The similar results have been also found in $MoSe_2/In_2S_3$ VSHs.

3.3 Polarization-tuned carrier density and spatial distribution in TMD/In_2X_3 VSHs

To qualitatively describe the polarization-induced self-doping effect in TMD/In_2X_3 VSHs, the carrier density of $MoTe_2/In_2Se_3$ VSHs in two polarization states have been calculated. The density of electrons (σ_n) and holes (σ_p) of the VSHs in P_{up} and P_{down} states as a function of temperature are plotted in Figs. 7(a) and (b), respectively. The intrinsic carrier density of $MoTe_2$ monolayer has been also provided for the comparison. For $MoTe_2/In_2Se_3$(↑) VSHs [Fig. 7(a)], the σ_n and σ_p are sensitive to the variation of In_2Se_3 layer. For instance, σ_n increases from ~10^{-2} to 4.3 × 10^{13} cm^{-2} and σ_p increases from ~10^6

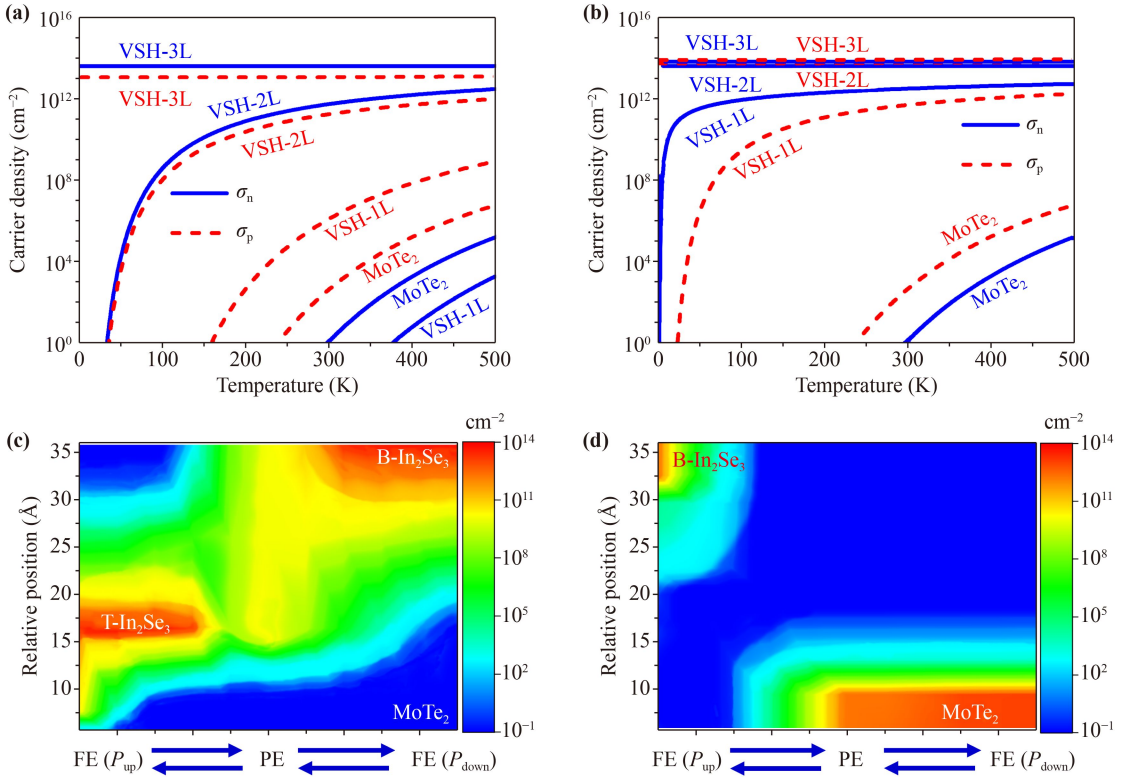

Fig. 7 Polarization-dependent carrier density in 2D $MoTe_2/In_2Se_3$ VSHs. The σ_n (solid lines) and σ_p (dash lines) of $MoTe_2/In_2Se_3$ VSHs in **(a)** P_{up} state and **(b)** P_{down} state. The VSH-nL (n = 1–3) denote the $MoTe_2/In_2Se_3$ VSH with nL-In_2Se_3 layer. The spatial distribution of **(c)** σ_n and **(d)** σ_p in $MoTe_2$/3L-In_2Se_3 VSH along the FE switching pathway from the P_{up} state, PE phase, to P_{down} state.

to 1.2 × 10^{13} cm^{-2} with the thickness increase of In_2Se_3 layer from 1L to 3L at the room temperature (298 K). Here it needs to be mentioned that the further increase of In_2Se_3 layer (e.g., >3L) does not significantly change the σ_n and σ_p values due to the Fermi-level pinning induced by the crossover of band-edge states mentioned above. In contrast, the carrier density of $MoTe_2/In_2Se_3(\downarrow)$ VSHs displays a relatively smaller change with the variation of In_2Se_3 layer. Moreover, the carrier density of the VSHs is not very sensitive to the temperature change [Fig. 7(b)]. For example, σ_n largely keeps at 2.1 × 10^{12}, 4.2 × 10^{13}, and 6.7 × 10^{13} cm^{-2} and σ_n basically maintains at 1.6 × 10^{11}, 4.8 × 10^{13}, and 8.3 × 10^{13} cm^{-2} for the VSH with 1L-, 2L-, and 3L-In_2Se_3, respectively. The results originate from the formation of tunneling p–n junctions [Fig. 5(d)] where the carrier transport is dominated by the tunneling mechanism [57]. The similar result has been demonstrated in the tunneling BP/ReS_2 p–n heterojunctions [58]. Moreover, the carrier density of $MoTe_2/In_2Se_3$ VSHs is far larger than that of the pristine $MoTe_2$ (< 10^6 cm^{-2}). Importantly, the doping level in TMD/In_2X_3 VSHs induced by the local FE polarization exceeds most of electrically and chemically modified TMD junctions, including lateral $MoTe_2$ homojunction [(3–5) × 10^{12} cm^{-2}] [59], $MoTe_2/MoS_2$ VSHs (10^{11}–10^{12} cm^{-2}) [60], lateral $WSe_2/MoSe_2$ heterojunctions (10^{11} cm^{-2}) [61], and WSe_2/MoS_2 VSHs (~10^{12} cm^{-2}) [62].

In addition to the promotion of carrier density, the polarization switching can be also used to manipulate the carrier spatial distribution of TMD/In_2X_3 VSHs. For example, the electrons and holes of $MoTe_2/In_2Se_3(\uparrow)$ tend to be localized at T-In_2Se_3 and B-In_2Se_3 layers, respectively. While the polarization switching into P_{down} state leads to the carrier separation into the $MoTe_2$ and B-In_2Se_3 layers. In order to better insight into the evolution of carrier spatial distribution in TMD/In_2X_3 VSHs during the polarization switching, we used $MoTe_2$/3L-In_2Se_3 VSH as an example and plotted its spatial distribution of carrier density isosurfaces along the phase transition pathway from the P_{up} state to the PE state to the P_{down} state, as shown in Figs. 7(c) and (d). The corresponding band structure evolution of $MoTe_2$ and In_2Se_3 layers in the VSH associated to the sequential phase switching has been presented in Fig. S9. When the polarization state transforms from the P_{up} state to the PE state, the FE polarization of In_2Se_3 layer will be gradually reduced to zero. The layer-by-layer band shift in the In_2Se_3 layer is weakened and the band-edge-states of $MoTe_2$ layer indicate an upward shift in this process (Fig. S9 in the ESM). Hence, we observe the electron delocalization from the T-In_2Se_3 layer to the whole

In_2Se_3 layer [Fig. 7(c)] and the hole localization from the B-In_2Se_3 layer to the $MoTe_2$ layer [Fig. 7(d)], respectively. The decreased FE polarization leads to the reduction of σ_n and σ_n in this process due to the carrier delocalization and band shift. When the polarization state transforms from the PE state to the P_{down} state, the FE polarization of In_2Se_3 layer will be gradually enhanced. The band-edge states of In_2Se_3 layer are changed from degenerate into dispersed with a layer-by-layer shift (Fig. S9 in the ESM), promoting the electron localization in the B-In_2Se_3 layer. The enhanced polarization and band bending are responsible for the increase of σ_n and σ_n in the process [Figs. 7(c) and (d)]. The results suggest that the carrier density and spatial distribution of TMD/In_2X_3 VSHs can be simultaneously modulated by the FE polarization switching.

4 Conclusions

In summary, we have theoretically demonstrated the feasibility to modulate the band alignment and spatial carrier density of 2D TMD/In_2X_3 VSHs via switchable FE polarization. Our calculated results indicate that the layer-by-layer band shift of In_2X_3 layer driven by the FE polarization field induces TMD/In_2X_3 VSHs with tunable band alignments and doping polarities, which enables us to manipulate the carrier type and density in the VSHs by the control of polarization orientation and magnitude. Based on this strategy, nonvolatile vdW p–n junctions have been achieved in $MoTe_2/In_2Se_3$ VSHs with ultrahigh carrier density (10^{13}–10^{14} cm^{-2}). Moreover, the switching of FE polarization from P_{up} to P_{down} state can lead to the transition of the VSHs from n–p junctions to p–i–n junctions. This work provides a new doping strategy for modulating the carrier type and density of 2D VSHs without any structural damages, paving the way for exploiting versatile 2D electronics and optoelectronics.

Electronic supplementary materials Supplementary materials (interfacial configurations and stabilities of 2D TMD/In_2X_3 VSHs, electrostatic potentials and band structures of 2D α-In_2X_3 nanosheets, thickness effect on projected band structures of $MoTe_2/In_2Se_3$ VSHs, band alignments of $MoSe_2/In_2S_3$ VSHs, and the band evoltion of In_2Se_3 and $MoTe_2$ layer in $MoTe_2/In_2Se_3$ VSHs associated to the ferroelectric phase transition) are available in the online version of this article at http://doi.org/10.1007/s11467-022-1244-4 and https://journal.hep.com.cn/fop/EN/10.1007/s11467-022-1244-4.

Acknowledgements This work was supported by the National Natural Science Foundation of China (Grant No. 62174151 and 61775201) and the Fund of Zhejiang Provincial Natural Science Foundation of China (Grant No. LZ22F040003 and LY22A040002). Computational resources from the Shanghai Supercomputer Center are acknowledged.

References

1. J. Simon, V. Protasenko, C. Lian, H. Xing, and D. Jena, Polarization-induced hole doping in wide-band-gap uniaxial semiconductor heterostructures, *Science* 327(5961), 60 (2010)
2. J. D. Sau, R. M. Lutchyn, S. Tewari, and S. Das Sarma, Generic new platform for topological quantum computation using semiconductor heterostructures, *Phys. Rev. Lett.* 104(4), 040502 (2010)
3. C. Siegert, A. Ghosh, M. Pepper, I. Farrer, and D. A. Ritchie, The possibility of an intrinsic spin lattice in high-mobility semiconductor heterostructures, *Nat. Phys.* 3(5), 315 (2007)
4. J. Narayan and S. Oktyabrsky, Formation of misfit dislocations in thin film heterostructures, *J. Appl. Phys.* 92(12), 7122 (2002)
5. X. Liu, D. Cao, Y. Yao, P. Tang, M. Zhang, X. Chen, and H. Shu, Heteroepitaxial growth and interface band alignment in a large-mismatch $CsPbI_3$/GaN heterojunction, *J. Mater. Chem. C* 10(6), 1984 (2022)
6. R. Yang, J. Fan, and M. Sun, Transition metal dichalcogenides (TMDCs) heterostructures: Optoelectric properties, *Front. Phys.* 17(4), 43202 (2022)
7. K. Mak and J. Shan, Photonics and Optoelectronics of 2D semiconductor transition metal dichalcogenides, *Nat. Photonics* 10(4), 216 (2016)
8. H. Liu, Y. Du, Y. Deng, and P. D. Ye, Semiconducting black phosphorus: synthesis, transport properties and electronic applications, *Chem. Soc. Rev.* 44(9), 2732 (2015)
9. S. Zhang, S. Guo, Z. Chen, Y. Wang, H. Gao, J. Gómez-Herrero, P. Ares, F. Zamora, Z. Zhu, and H. Zeng, Recent progress in 2D group-VA semiconductors: from theory to experiment, *Chem. Soc. Rev.* 47(3), 982 (2018)
10. Y. Liu, N. O. Weiss, X. Duan, H. C. Cheng, Y. Huang, and X. Duan, Van der Waals heterostructures and devices, *Nat. Rev. Mater.* 1(9), 16042 (2016)
11. Y. Y. Wang, F. P. Li, W. Wei, B. B. Huang, and Y. Dai, Interlayer coupling effect in van der Waals heterostructures of transition metal dichalcogenides, *Front. Phys.* 16(1), 13501 (2021)
12. L. Zhang, Z. Zhang, F. Wu, D. Wang, R. Gogna, S. Hou, K. Watanabe, K. Taniguchi, K. Kulkarni, T. Kuo, S. R. Forrest, and H. Deng, Twist-angle dependence of moiré excitons in $WS_2/MoSe_2$ heterobilayers, *Nat. Commun.* 11(1), 5888 (2020)
13. M. R. Rosenberger, H. J. Chuang, M. Phillips, V. P. Oleshko, K. M. McCreary, S. V. Sivaram, C. S. Hellberg, and B. T. Jonker, Twist angle-dependent atomic reconstruction and moiré patterns in transition metal dichalcogenide heterostructures, *ACS Nano* 14(4), 4550 (2020)
14. H. Chen, X. Wen, J. Zhang, T. Wu, Y. Gong, X. Zhang, J. Yuan, C. Yi, J. Lou, P. M. Ajayan, W. Zhuang, G. Zhang, and J. Zheng, Ultrafast formation of interlayer hot excitons in atomically thin MoS_2/WS_2 heterostructures, *Nat. Commun.* 7(1), 12512 (2016)
15. A. F. Rigosi, H. M. Hill, Y. Li, A. Chernikov, and T. F.

Heinz, Probing interlayer interactions in transition metal dichalcogenide heterostructures by optical spectroscopy: MoS_2/WS_2 and $MoSe_2/WSe_2$, *Nano Lett.* 15(8), 5033 (2015)
16. J. Guo, L. Wang, Y. Yu, P. Wang, Y. Huang, and X. Duan, $SnSe/MoS_2$ van der Waals heterostructure junction field-effect transistors with nearly ideal subthreshold slope, *Adv. Mater.* 31(49), 1902962 (2019)
17. Y. Cheng, P. Tang, P. Liang, X. Liu, D. Cao, X. Chen, and H. Shu, Sulfur-driven transition from vertical to lateral growth of 2D SnS–SnS_2 heterostructures and their band alignments, *J. Phys. Chem. C* 124(50), 27820 (2020)
18. J. Xu, J. Jia, S. Lai, J. Ju, and S. Lee, Tunneling field effect transistor integrated with black phosphorus-MoS_2 junction and ion gel dielectric, *Appl. Phys. Lett.* 110(3), 033103 (2017)
19. S. J. Liang, B. Cheng, X. Cui, and F. Miao, Van der Waals heterostructures for high-performance device applications: Challenges and opportunities, *Adv. Mater.* 32, 1903800 (2020)
20. R. Cheng, F. Wang, L. Yin, Z. Wang, Y. Wen, T. A. Shifa, and J. He, High-performance, multifunctional devices based on asymmetric van der Waals heterostructures, *Nat. Electron.* 1(6), 356 (2018)
21. H. P. Komsa, J. Kotakoski, S. Kurasch, O. Lehtinen, U. Kaiser, and A. V. Krasheninnikov, Two-dimensional transition metal dichalcogenides under electron irradiation: Defect production and doping, *Phys. Rev. Lett.* 109(3), 035503 (2012)
22. Q. Zhang, H. Ying, X. Li, R. Xiang, Y. Zheng, H. Wang, J. Su, M. Xu, X. Zheng, S. Maruyama, and X. Zhang, Controlled doping engineering in 2D MoS_2 crystals toward performance augmentation of optoelectronic devices, *ACS Appl. Mater. Interfaces* 13(27), 31861 (2021)
23. Y. Gong, H. Yuan, C. L. Wu, P. Tang, S. Z. Yang, A. Yang, G. Li, B. Liu, J. van de Groep, M. L. Brongersma, M. F. Chisholm, S. C. Zhang, W. Zhou, and Y. Cui, Spatial controlled doping of two-dimensional SnS_2 through intercalation for electronics, *Nat. Nanotechnol.* 13(4), 294 (2018)
24. D. Kiriya, M. Tosun, P. Zhao, J. S. Kang, and A. Javey, Air-stable surface charge transfer doping of MoS_2 by benzyl viologen, *J. Am. Chem. Soc.* 136(22), 7853 (2014)
25. W. Shi, S. Kahn, L. Jiang, S. Y. Wang, H. Z. Tsai, D. Wong, T. Taniguchi, K. Watanabe, F. Wang, M. F. Crommie, and A. Zettl, Reversible writing of high mobility and high-carrier density doping patterns in two-dimensional van der Waals heterostructures, *Nat. Electron.* 3(2), 99 (2020)
26. R. Zhang, Z. Xie, C. An, S. Fan, Q. Zhang, S. Wu, L. Xu, X. Hu, D. Zhang, D. Sun, J. Chen, and J. Liu, Ultraviolet light-induced persistent and degenerated doping in MoS_2 for potential photocontrollable electronics applications, *ACS Appl. Mater. Interfaces* 10(33), 27840 (2018)
27. M. Buscema, D. J. Groenendijk, G. A. Steele, H. S. J. van der Zant, and A. Castellanos-Gomez, Photovoltaic effect in few-layer phosphorus PN junctions defined local electrostatic gating, *Nat. Commun.* 5(1), 4651 (2014)
28. P. Agnihotri, P. Dhakras, and J. U. Lee, Bipolar junction transistors in two-dimensional WSe_2 with large current and photocurrent grains, *Nano Lett.* 16(7), 4355 (2016)
29. S. J. Lee, Z. Lin, X. Duan, and Y. Huang, Doping on demand in 2D devices, *Nat. Electron.* 3(2), 77 (2020)
30. L. Kong, X. Zhang, Q. Tao, M. Zhang, W. Dang, Z. Li, L. Feng, L. Liao, X. Duan, and Y. Liu, Doping-free complementary WSe_2 circuit via van der Waals metal integration, *Nat. Commun.* 11(1), 1866 (2020)
31. D. Wijethunge, L. Zhang, C. Tang, and A. Du, Tunning band alignment and optical properites of 2D van der Waals heterostructure via ferroelectric polarization switching, *Front. Phys.* 15(6), 63504 (2020)
32. J. W. Chen, S. T. Lo, S. C. Ho, S. S. Wong, T. H. Y. Vu, X. Q. Zhang, Y. D. Liu, Y. Y. Chiou, Y. X. Chen, J. C. Yang, Y. C. Chen, Y. H. Chu, Y. H. Lee, C. J. Chung, T. M. Chen, C. H. Chen, and C. L. Wu, A gate-free monolayer WSe_2 PN diode, *Nat. Commun.* 9(1), 3143 (2018)
33. Z. Lu, C. Serrao, A. I. Khan, L. You, J. C. Wong, Y. Ye, H. Zhu, X. Zhang, and S. Salahuddin, Nonvolatile MoS_2 field effect transistors directly gated by single crystalline epitaxial ferroelectric, *Appl. Phys. Lett.* 111(2), 023104 (2017)
34. A. Nguyen, P. Sharma, T. Scott, E. Preciado, V. Klee, D. Sun, I. H. D. Lu, D. Barroso, S. H. Kim, V. Y. Shur, A. R. Akhmatkhanov, A. Gruverman, L. Bartels, and P. A. Dowben, Toward ferroelectric control of monolayer MoS_2, *Nano Lett.* 15(5), 3364 (2015)
35. X. Liu, X. Zhou, Y. Pan, J. Yang, H. Xiang, Y. Yuan, S. Liu, H. Luo, D. Zhang, and J. Sun, Charge–ferroelectric transition in ultrathin $Na_{0.5}Bi_{4.5}Ti_4O_{15}$ flakes probed via a dual-gated full van der Waals transistor, *Adv. Mater.* 32(49), 2004813 (2020)
36. G. Wu, X. Wang, Y. Chen, S. Wu, B. Wu, Y. Jiang, S. Shen, T. Lin, Q. Liu, X. Wang, P. Zhou, S. Zhang, W. Hu, X. Meng, J. Chu, and J. Wang, $MoTe_2$ p–n homojunctions defined by ferroelectric polarization, *Adv. Mater.* 32(16), 1907937 (2020)
37. G. Wu, B. Tian, L. Liu, W. Lv, S. Wu, X. Wang, Y. Chen, J. Li, Z. Wang, S. Wu, H. Shen, T. Lin, P. Zhou, Q. Liu, C. Duan, S. Zhang, X. Meng, S. Wu, W. Hu, X. Wang, J. Chu, and J. Wang, Programmable transition metal dichalcogenide homojunctions controlled by nonvolatile ferroelectric domains, *Nat. Electron.* 3(1), 43 (2020)
38. N. A. Spaldin, Fundamental size limits in ferroelectricity, *Science* 304(5677), 1606 (2004)
39. M. Dawber, K. M. Rabe, and J. F. Scott, Physics of thin-film ferroelectric oxides, *Rev. Mod. Phys.* 77(4), 1083 (2005)
40. A. Belianinov, Q. He, A. Dziaugys, P. Maksymovych, E. Eliseev, A. Borisevich, A. Morozovska, J. Banys, Y. Vysochanskii, and S. V. Kalinin, $CuInP_2S_6$ room temperature layered ferroelectric, *Nano Lett.* 15(6), 3808 (2015)
41. W. Ding, J. Zhu, J. Wang, Y. Gao, D. Xiao, Y. Gu, Z. Zhang, and W. Zhu, Prediction of intrinsic two-dimensional frroelectrics in In_2Se_3 and other III_2–VI_3 van der

Waals materials, *Nat. Commun.* 8(1), 14956 (2017)
42. N. Higashitarumizu, H. Kawamoto, C. J. Lee, B. H. Lin, F. H. Chu, I. Yonemori, T. Nishimura, K. Wakabayashi, W. Chang, and K. Nagashio, Purely in-plane ferroelectricity in monolayer SnS at room temperature, *Nat. Commun.* 11(1), 2428 (2020)
43. S. Yuan, X. Luo, H. L. Chan, C. Xiao, Y. Dai, M. Xie, and J. Hao, Room-temperature ferroelectricity in $MoTe_2$ down to the atomic monolayer limit, *Nat. Commun.* 10(1), 1775 (2019)
44. F. Xue, W. Hu, K. C. Lee, L. S. Lu, J. Zhang, H. L. Tang, A. Han, W. T. Hsu, S. Tu, W. H. Chang, C. H. Lien, J. H. He, Z. Zhang, L. J. Li, and X. Zhang, Room-temperature ferroelectricity in hexagonally layered α-In_2Se_3 nanoflakes down to the monolayer limit, *Adv. Funct. Mater.* 28(50), 1803738 (2018)
45. J. Quereda, R. Biele, G. Rubio-Bollinger, N. Agrait, R. D'Agosta, and A. Castellanos-Gomez, Strong quantum confinement effect in the optical properties of ultrathinα-In_2Se_3, *Adv. Opt. Mater.* 4(12), 1939 (2016)
46. M. Yang, H. Shu, Y. Li, D. Cao, and X. Chen, Polarization-induced band alignment transition and nonvolatile p–n junctions in 2D van der Waals heterostructures, *Adv. Electron. Mater.* 8(3), 2101022 (2022)
47. G. Kresse and J. Furthmüller, Efficient iterative schemes for *ab initio* total-energy calculations using a plane-wave basis set, *Phys. Rev. B* 54(16), 11169 (1996)
48. M. C. Payne, M. P. Teter, D. C. Allan, T. A. Arias, and J. D. Joannopoulos, Iterative minimization techniques for ab initio total-energy calculations: Molecular dynamics and conjugate gradients, *Rev. Mod. Phys.* 64(4), 1045 (1992)
49. S. Grimme, Semiempirical GGA-type density functional constructed with a long-range dispersion correction, *J. Comput. Chem.* 27(15), 1787 (2006)
50. J. Heyd, G. E. Scuseria, and M. Ernzerhof, Hybrid functionals based on a screened coulomb potential, *J. Chem. Phys.* 118(18), 8207 (2003)
51. R. D. King-Smith and D. Vanderbilt, Theory of polarization of crystalline solids, *Phys. Rev. B* 47(3), 1651 (1993)
52. R. F. Bader, A quantum theory of molecular structure and its applications, *Chem. Rev.* 91(5), 893 (1991)
53. W. F. Io, S. Yuan, S. Y. Pang, L. W. Wong, J. Zhao, and J. Hao, Temperature- and thickness-dependence of robust out-of-plane ferroelectricity in CVD grown ultrathin van der Waals α-In_2Se_3 layers, *Nano Res.* 13(7), 1897 (2020)
54. R. Peng, Y. Ma, S. Zhang, B. Huang, L. Kou, and Y. Dai, Self-doped p–n junctions in two-dimensional In_2X_3 van der Waals materials, *Mater. Horiz.* 7(2), 504 (2020)
55. T. Björkman, A. Gulans, A. V. Krasheninnikov, and R. M. Nieminen, Van der Waals bonding in layered compounds from advanced density-functional first-principles calculations, *Phys. Rev. Lett.* 108(23), 235502 (2012)
56. M. Yang, H. Shu, P. Tang, P. Liang, D. Cao, and X. Chen, Intrinsic polarization-induced enhanced ferromagnetism and self-doped p–n junctions in $CrBr_3$/GaN van der Waals heterostructures, *ACS Appl. Mater. Interfaces* 13(7), 8764 (2021)
57. P. J. Jeon, Y. T. Lee, J. Y. Lim, J. S. Kim, D. K. Hwang, and S. Im, Black phosphorus–zinc oxide nanomaterial heterojunction for p–n diode and junction field-effect transistor, *Nano Lett.* 16(2), 1293 (2016)
58. P. K. Srivastava, Y. Hassan, Y. Gebredingle, J. Jung, B. Kang, W. J. Yoo, B. Singh, and C. Lee, Van der waals broken-gap p–n heterojunction tunnel diode based on black Phosphorus and rhenium disulfide, *ACS Appl. Mater. Interfaces* 11(8), 8266 (2019)
59. D. Qu, X. Liu, M. Huang, C. Lee, F. Ahmed, H. Kim, R. S. Ruoff, J. Hone, and W. J. Yoo, Carrier-type modulation and mobility improvement of thin $MoTe_2$, *Adv. Mater.* 29(39), 1606433 (2017)
60. Y. Xie, E. Wu, S. Fan, G. Geng, X. Hu, L. Xu, S. Wu, J. Liu, and D. Zhang, Modulation of $MoTe_2/MoS_2$ van der Waals heterojunctions for multifunctional devices using N_2O plasma with an opposite doping effect, *Nanoscale* 13(16), 7851 (2021)
61. J. E. Kim, W. T. Kang, V. Tu Vu, Y. R. Kim, Y. S. Shin, I. Lee, U. Y. Won, B. H. Lee, K. Kim, T. L. Phan, Y. H. Lee, and W. J. Yu, Ideal PN photodiode using doping controlled WSe_2–$MoSe_2$ lateral heterostructure, *J. Mater. Chem. C* 9(10), 3504 (2021)
62. C. H. Lee, G. H. Lee, A. M. van der Zande, W. Chen, Y. Li, M. Han, X. Cui, G. Arefe, C. Nuckolls, T. F. Heinz, J. Guo, J. Hone, and P. Kim, Atomically thin p–n junctions with van der Waals heterointerfaces, *Nat. Nanotechnol.* 9(9), 676 (2014)